Correction for the Dislocation of Curved Surfaces Caused by the PSF in 2D and 3D CT Images

Henri Bouma, Anna Vilanova, Lucas J. van Vliet, and Frans A. Gerritsen

Abstract—Conventional edge-detection methods suffer from the dislocation of curved surfaces due to the PSF. We propose a new method that uses the isophote curvature to circumvent this. It is accurate for objects with locally constant curvature, even for small objects (like blood vessels) and in the presence of noise.

Index Terms—Edge and feature detection.

1 Introduction

MANY clinical applications of medical imaging require that edges be accurately located. An example is the diagnosis of a vascular disease, where the grading of stenoses is an important factor in determining the treatment therapy [1]. However, inherent to the acquisition step is a blurring effect, which can be modeled by the convolution with a *point-spread function* (PSF). This blurring function causes conventional edge-detection methods to inaccurately locate edges, leading to errors in quantification and visualization.

The dislocation of curved edges due to the PSF was shown several times in the literature. Vessel quantification measurements have shown that an adaptive threshold causes an error in the diameter estimation of cylindrical structures [1], [2], [3]. Frangi et al. [1] and Krissian et al. [4] used a simplified model to approximate the cross-section of a tube. Later, Krissian et al. [5] showed that the radius estimation of tubes in CT images can be improved by modeling the PSF correctly.

Many deconvolution methods have been proposed to undo the blurring caused by the PSF, which include approximations of the inverse filter and iterative methods [6]. Most deconvolution methods are ill-posed and, hence, unstable and noise enhancing, which deteriorates the result [7]. Regularization can be used to reduce the sensitivity to noise at the expense of a considerable increase in computational cost for iterative methods [8].

We propose a new noniterative edge-localization method that yields an exact correspondence between the edge that is detected and the true surface of objects in the real word. The locally measured isophote curvature is used to correct for the dislocation of the curved surface due to Gaussian blurring, in 2D and 3D [9]. The analysis in this paper and the proposed method are applicable where the images show rather homogeneous objects and where the PSF can be approximated by a Gaussian. Although the PSF is not completely isotropic and shift invariant for computed tomography (CT) [12], this approximation can safely be made for CT and several other medical acquisition modalities [10].

This paper is organized as follows: In Section 2, existing methods for edge detection are summarized. In Section 3, the dislocation of curved edges is analyzed mathematically. An approximation for curved surfaces in 3D is made in Section 4. Section 5 is about the implementation of the proposed method. Finally, in Section 6, experimental results are discussed.

- *H. Bouma and A. Vilanova are with the Department of Biomedical Engineering, Technische Universiteit Eindhoven, Postbus 513, 5600 MB Eindhoven, The Netherlands. E-mail: {h.bouma2, a.vilanova}@tue.nl.*
- *L.J. van Vliet is with the Quantitative Imaging Group, Faculty of Applied Sciences, Delft University of Technology, Postbus 5, 2600 AA Delft, The Netherlands. E-mail: l.j.vanvliet@ph.tn.tudelft.nl.*
- *F.A. Gerritsen is with the Department of Biomedical Engineering, Technische Universiteit Eindhoven, Postbus 513, 5600 MB Eindhoven, The Netherlands and is also with Philips Medical Systems, Postbus 10000, 5680 DA Best, The Netherlands. E-mail: Frans.Gerritsen@philips.com.*

Manuscript received 24 Mar. 2004; revised 17 Feb. 2005; accepted 17 Feb. 2005; published online 14 July 2005.
Recommended for acceptance by A. Rangarajan.
For information on obtaining reprints of this article, please send e-mail to: tpami@computer.org, and reference IEEECS Log Number TPAMI-0144-0304.

2 Existing Edge-Detection Methods

Object boundaries are usually detected with first and second-order derivatives. The gradient, i.e., a vector of first-order derivatives, may indicate the presence of an edge and the maximum of the gradient magnitude is commonly used to locate edges. The zero-crossings of the second-order derivative in the gradient direction (L_{ww}) are located where the gradient magnitude is maximal [13]. For simplicity, the zero crossings of the Laplacian (ΔL) can also be used to locate edges [14]. The Laplacian is easy to calculate, but the zero crossings are not located where the gradient is maximal [15], [16]. However, our goal is not to find the position of maximal gradient in the blurred image, but to find the location of the edge before blurring. For example, if the edge of a circular object with radius R is not defined as the position where the gradient is maximal after blurring, but as the location before blurring, the zero-crossing positions r_0 of both methods (ΔL and L_{ww}) give a dislocation of the curved edges. The dislocation $(r_0 - R)$ of these methods goes in opposite directions (Fig. 1). ΔL gives an overestimation and L_{ww} gives an underestimation of the radius. The dislocation is caused by the isophote curvature κ in relation to the standard deviation σ of the Gaussian blurring. Since both ΔL and L_{ww} appear to be dislocated in opposite directions, Verbeek and van Vliet [18] proposed the *PLUS* operator, which sums ΔL with L_{ww}. This operator reduces the dislocation of curved edges. Mendonça et al. [17] recently proposed a two-step method that fits a curve through the zero crossings of L_{ww} and corrects for the bias in the localization by shifting the curve according to the dislocation that is known if the curvature is locally constant. We will derive a filtering method that corrects for the dislocation and does not require curve extraction. The methods are analyzed in the next section.

3 Analysis of Curved Edges and Surfaces

In this section, the dislocation of edge detectors is mathematically analyzed and a new operator is derived. The zero crossings of this operator are located exactly at surfaces with locally constant curvature. First, the notation, assumptions, and problem definition are mentioned. The filter is derived for 2D and 3D in Sections 3.4 and 3.5, respectively. Finally, at the end of this section, conclusions will be drawn.

3.1 Background and Notation

Partial derivatives will be denoted by subscripts, as in M_x for $\frac{\partial M}{\partial x}$ or L_{yy} for $\frac{\partial^2 L}{\partial y^2}$.

Derivatives are calculated in a locally fixed coordinate system (gauge coordinates). The vector w is defined in the direction of the gradient and vector v (and u, in 3D) are perpendicular to w. Thus, L_{ww} is the second-order derivative in the gradient direction. The first order derivative in the gradient direction (L_w) is equal to the gradient magnitude and the first-order derivative tangential to the isosurface (L_v) is equal to zero.

The isophote curvature in 2D is denoted by κ. In 3D, it consists of two values (the principal curvatures, κ_1 and κ_2, sorted by magnitude, $|\kappa_1| > |\kappa_2|$). The vectors corresponding to these values are perpendicular to the gradient and perpendicular to each other. The sum of principal curvatures will be denoted as $\kappa_\Sigma\,(= \kappa_1 + \kappa_2)$.

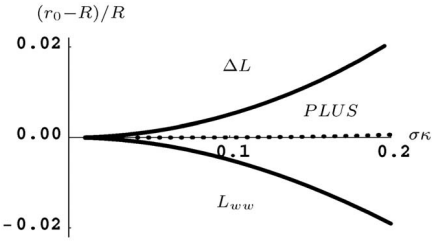

Fig. 1. The zero-crossings r_0 of the Laplacian (ΔL) and the second-order derivative in the gradient direction (L_{ww}) are dislocated in the opposite direction. Therefore, the *PLUS* operator ($\Delta L + L_{ww}$) was proposed by Verbeek and van Vliet [18].

3.2 Assumptions

Three assumptions are made during the derivation.

3.2.1 Homogeneous

Regions are rather homogeneous. Therefore, edges can be modeled by the Heaviside unit step $\mathcal{U}(x)$.

3.2.2 Constant Curvature

The curvature is assumed to be locally constant. Locally constant curvature means that the curvature is constant inside the footprint of the blurring function. The unblurred objects $M = \mathcal{U}(R - r)$ with constant curvature will be a disk (interior of circle) in 2D, a ball (solid sphere) and a cylinder in 3D with radial coordinate r (distance to the origin) and radius R.

3.2.3 Gaussian PSF

The shape of the PSF, which causes the blurring, is assumed to be Gaussian:

$$\mathcal{G} = \frac{1}{(\sqrt{2\pi\sigma^2})^N} exp\left(-\frac{\vec{r}.\vec{r}}{2\sigma^2}\right), \tag{1}$$

where σ is the standard deviation, N is the number of dimensions, and $(\vec{r}.\vec{r})$ is the dot product of the position vector with itself. In Cartesian coordinates, the position vector $\vec{r} = [x, y, z]^T$.

The blurred object L is defined as an N-dimensional convolution: $L = M * \mathcal{G}$.

3.3 Problem Definition

The most commonly used edge detectors are the detectors of Canny [13] and Marr-Hildreth [14] based on L_{ww} and ΔL, respectively. Fig. 1 shows that both dislocate the edges in opposite directions. The *PLUS* operator ($L_{ww} + \Delta L$) results in an edge detector with a better localization. However, if $\sigma\kappa$ is larger than 0.2, the performance of the *PLUS* operator also diminishes (as shown in Section 6). The equation of the *PLUS* operator in 2D can be written as:

$$PLUS = L_{ww} + \Delta L = 2\left(L_{ww} - \frac{1}{2}\kappa\, L_w\right). \tag{2}$$

We want to correct for the dislocation of curved surfaces. Therefore, we use the curvature term in (2) to obtain a better localization. This can be achieved by solving:

$$L_{ww} - \alpha(\sigma\,\kappa)\ \kappa\, L_w = 0 \tag{3}$$

for the function $\alpha(\sigma\,\kappa)$, where $\alpha(\sigma\,\kappa)$ is expected to be approximately 0.5 for small values of $\sigma\,\kappa$ (like the *PLUS* operator). The product of the standard deviation of the Gaussian blurring σ and the local isophote curvature κ is taken as the parameter of this function $\alpha(\sigma\,\kappa)$ because it is a dimensionless quantity and, therefore, scale invariant.

3.4 Curved Edges in 2D

The simplest object with (locally) constant curvature in 2D, is a disk $M = \mathcal{U}(R - r)$. The position vector, expressed in polar coordinates, is: $\vec{r} = [r\,cos(\phi),\, r\,sin(\phi)]^T$. The derivatives of M are:

$$\begin{aligned}
M_x &= -cos(\phi)\delta(R-r)\\
M_y &= -sin(\phi)\delta(R-r)\\
M_w &= \sqrt{M_x^2 + M_y^2} = \delta(R-r)\\
M_{ww} &= \frac{M_x^2 M_{xx} + 2M_x M_{xy} M_y + M_y^2 M_{yy}}{M_x^2 + M_y^2} = \delta'(R-r)\\
\Delta M &= M_{xx} + M_{yy} = \delta'(R-r) - \frac{\delta(R-r)}{r}.
\end{aligned} \tag{4}$$

The gradient magnitude of the blurred object L_w can be obtained by the convolution of M_w with a Gaussian $\mathcal{G}$. The final equations are rotation invariant. Therefore, we may choose $L_y = 0$ and $L_w = |L_x|$ without loss of generality.

$$\begin{aligned}
L_x &= M_x * \mathcal{G}\\
&= \int_0^\infty \int_0^{2\pi} \rho M_x(\vec{\rho})\mathcal{G}(\vec{r}-\vec{\rho})d\Phi\, d\rho\\
&= \int_0^\infty \int_0^{2\pi} -\rho\, cos(\Phi)\,\delta(R-\rho)\\
&\quad \left(\frac{1}{2\pi\sigma^2} e^{-\frac{\rho^2+r^2-2r\rho\,cos(\phi-\Phi)}{2\sigma^2}}\right) d\Phi\, d\rho\\
&= -R\,\frac{1}{2\pi\sigma^2}\, e^{-\frac{R^2+r^2}{2\sigma^2}}\\
&\quad \int_0^{2\pi} cos(\Phi) e^{\frac{rR\,cos(\phi-\Phi)}{\sigma^2}} d\Phi\\
L_w &= \frac{R}{\sigma^2}\, e^{-\frac{R^2+r^2}{2\sigma^2}} I_1\left(\frac{rR}{\sigma^2}\right),
\end{aligned} \tag{5}$$

where $I_n(\cdot)$ is the modified Bessel function of the first kind. L_{ww} can be derived from L_w. These results are in agreement with the result of Mendonça et al. [17]. As shown in (4), ΔL can be calculated from L_w and L_{ww}.

$$\begin{aligned}
L_{ww} &= e^{-\frac{r^2+R^2}{2\sigma^2}}\left(-\frac{R^2}{\sigma^4} I_0\left(\frac{rR}{\sigma^2}\right) + \left(\frac{r\,R}{\sigma^4} + \frac{R}{r\sigma^2}\right) I_1\left(\frac{rR}{\sigma^2}\right)\right)\\
\Delta L &= e^{-\frac{r^2+R^2}{2\sigma^2}}\left(-\frac{R^2}{\sigma^4} I_0\left(\frac{rR}{\sigma^2}\right) + \frac{r\,R}{\sigma^4} I_1\left(\frac{rR}{\sigma^2}\right)\right).
\end{aligned} \tag{6}$$

The curvature κ can be obtained from $\Delta L = L_{ww} + L_{vv} = L_{ww} - \kappa\, L_w$. Notice that $\kappa = 1/r$. Finally, an edge detector with zero crossings at position $r_0 = R$ can be defined, $L_{ww} - \alpha\,\kappa\, L_w = 0$, and this equation can be solved for α.

$$\begin{aligned}
\alpha &= 1 + \frac{r^2}{\sigma^2} - \frac{r\,R}{\sigma^2}\frac{I_0\left(\frac{rR}{\sigma^2}\right)}{I_1\left(\frac{rR}{\sigma^2}\right)}\\
&= 1 + \frac{R^2}{\sigma^2} - \frac{R^2}{\sigma^2}\frac{I_0\left(\frac{R^2}{\sigma^2}\right)}{I_1\left(\frac{R^2}{\sigma^2}\right)} \qquad (\text{at } r = R).
\end{aligned} \tag{7}$$

Curvature is inversely proportional to the radius. This can be used to define α as a function of $\sigma\,\kappa$:

$$\alpha(\sigma\,\kappa) = 1 + \left(\frac{1}{\sigma\kappa}\right)^2\left(1 - \frac{I_0\left(\left(\frac{1}{\sigma\kappa}\right)^2\right)}{I_1\left(\left(\frac{1}{\sigma\kappa}\right)^2\right)}\right). \tag{8}$$

This equation is shown in Fig. 2. If $\sigma\kappa$ approaches zero, then $\alpha = 0.5$ and our operator becomes the *PLUS* operator. For $\sigma\,\kappa > 0.5$, the entire object is inside the center part of the Gaussian PSF. The α in (8) avoids dislocation of the zero crossings for an object with locally constant curvature in 2D. So, the proposed method can locate the edge of a disk without a bias.

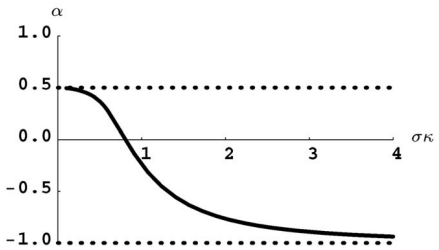

Fig. 2. Function α in (8) allows the localization of edges with locally constant curvature in 2D without a bias.

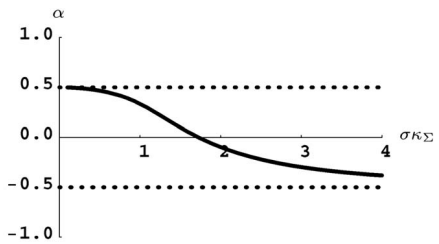

Fig. 3. Function α in (15) can be used to locate the edge of a ball in 3D without a bias.

3.5 Curved Surfaces in 3D

The curvature term of the *PLUS* operator in 3D depends on the sum of curvatures.

$$PLUS = 2\left(L_{ww} - \frac{1}{2}(\kappa_1 + \kappa_2)L_w\right). \tag{9}$$

Therefore, the κ in the 2D problem definition is replaced by the sum of curvatures κ_Σ in 3D:

$$L_{ww} - \alpha\,\kappa_\Sigma\,L_w = 0 \qquad (r = R). \tag{10}$$

Simple objects in 3D with constant curvature and different ratios of κ_2/κ_1 are balls ($\kappa_2/\kappa_1 = 1$) and cylinders ($\kappa_2/\kappa_1 = 0$). Both objects are described below.

3.5.1 Ball

The derivation for a ball is similar to that of a disk. The position vector, expressed in spherical coordinates is: $[r\,cos(\theta)sin(\phi), r\,sin(\theta)sin(\phi), r\,cos(\phi)]^T$. The derivatives of M are:

$$\begin{aligned}
M_x &= -cos(\theta)sin(\phi)\delta(R-r)\\
M_y &= -sin(\theta)sin(\phi)\delta(R-r)\\
M_z &= -cos(\phi)\delta(R-r)\\
M_w &= \sqrt{M_x^2 + M_y^2 + M_z^2} = \delta(R-r)\\
M_{ww} &= (M_x^2 M_{xx} + M_y^2 M_{yy} + M_z^2 M_{zz} +\\
&\quad 2(M_x(M_{xy}M_y + M_{xz}M_z) + M_y M_{yz} M_z))/\\
&\quad (M_x^2 + M_y^2 + M_z^2) = \delta'(R-r)\\
\Delta M &= M_{xx} + M_{yy} + M_{zz} = \delta'(R-r) - \frac{\delta(R-r)}{r}.
\end{aligned} \tag{11}$$

The gradient magnitude of the blurred object L_w can be calculated by a convolution. We choose $L_x = 0$, $L_y = 0$, and $L_w = |L_z|$ without loss of generality.

$$\begin{aligned}
L_z &= \int_0^\infty \int_0^\pi \int_0^{2\pi} \rho^2 sin(\Phi) M_z\, \mathcal{G}(\vec{r} - \vec{\rho})\, d\Theta d\Phi d\rho\\
&= -e^{-\frac{r^2+R^2}{2\sigma^2}} \frac{R\int_0^\pi sin(\Phi)\,cos(\Phi)\,e^{\frac{rR}{\sigma^2}\cos(\Phi)} d\Phi}{\sqrt{2\,\pi}\,\sigma^3}\\
L_w &= e^{-\frac{r^2+R^2}{2\sigma^2}} \frac{(r\,R + \sigma^2)e^{-\frac{rR}{\sigma^2}} + (r\,R - \sigma^2)\,e^{\frac{rR}{\sigma^2}}}{\sqrt{2\,\pi}\,r^2\,\sigma}.
\end{aligned} \tag{12}$$

L_{ww} can be derived from L_w, and ΔL from these two.

$$\begin{aligned}
L_{ww} &= \frac{e^{-\frac{(r+R)^2}{2\sigma^2}}}{\sqrt{2\pi}\,r^3\,\sigma^3}\left((r^3 R + 2rR\sigma^2)\left(1 + e^{\frac{2rR}{\sigma^2}}\right) +\right.\\
&\quad \left.(2\sigma^4 + r^2(R^2 + \sigma^2))\left(1 - e^{\frac{2rR}{\sigma^2}}\right)\right)\\
\Delta L &= e^{-\frac{(r+R)^2}{2\sigma^2}} \frac{rR\left(1 + e^{\frac{2rR}{\sigma^2}}\right) + (R^2 + \sigma^2)\left(1 - e^{\frac{2rR}{\sigma^2}}\right)}{\sqrt{2\pi}\,r\,\sigma^3}.
\end{aligned} \tag{13}$$

The sum of curvatures κ_Σ can be obtained with $\Delta L = L_{ww} - \kappa_\Sigma\,L_w$. Notice that the sum of curvatures on a ball is $\kappa_\Sigma = 2/r$, because each of the two principal components of isophote curvature is $1/r$. Finally, an edge detector with zero crossings at position $r = R$ can be defined, $L_{ww} - \alpha\,\kappa_\Sigma\,L_w = 0$, and this equation can be solved for α, resulting in:

$$\alpha = \frac{2\left(\frac{R}{\sigma}\right)^4 + 2\left(1 - e^{2\left(\frac{R}{\sigma}\right)^2}\right) + \left(\frac{R}{\sigma}\right)^2\left(3 + e^{2\left(\frac{R}{\sigma}\right)^2}\right)}{2\left(1 - e^{2\left(\frac{R}{\sigma}\right)^2} + \left(\frac{R}{\sigma}\right)^2\left(1 + e^{2\left(\frac{R}{\sigma}\right)^2}\right)\right)}. \tag{14}$$

Replacing R by $2/\kappa_\Sigma$ will define α to be a function of the product of κ_Σ and σ.

$$\alpha(\sigma\,\kappa_\Sigma) = \frac{2\left(\frac{2}{\sigma\kappa_\Sigma}\right)^4 + 2\left(1 - e^{2\left(\frac{2}{\sigma\kappa_\Sigma}\right)^2}\right) + \left(\frac{2}{\sigma\kappa_\Sigma}\right)^2\left(3 + e^{2\left(\frac{2}{\sigma\kappa_\Sigma}\right)^2}\right)}{2\left(1 - e^{2\left(\frac{2}{\sigma\kappa_\Sigma}\right)^2} + \left(\frac{2}{\sigma\kappa_\Sigma}\right)^2\left(1 + e^{2\left(\frac{2}{\sigma\kappa_\Sigma}\right)^2}\right)\right)}. \tag{15}$$

This equation is shown in Fig. 3. It can be used to locate the edge of a ball without a bias.

3.5.2 Cylinder

For a cylinder, the 3D Gaussian can be decomposed in one component in the direction of the central axis of a cylinder (z-direction) and two components in the cross-sectional plane. Because all derivatives in the z-direction are zero, the solution for the cylinder is identical to that of the disk after replacing the 2D κ by the 3D κ_Σ in (8). This function α is used to accurately quantify the diameter of tubular structures (such as blood vessels).

3.6 Conclusion of the Analysis

An unbiased edge detector was derived for blurred disks, balls, and cylinders. For small values of $\sigma\,\kappa$, function α approaches 0.5 and our operator approximates the *PLUS* operator, as expected. Increasing $\sigma\,\kappa$ yields different values for α. Instead of extracting a contour in 2D at the zero crossings of L_{ww} and estimating the required dislocation, as Mendonça et al. proposed [17], we designed an edge-detector with its zero-crossings at the correct location that can also be applied in 3D.

The analysis helps us to obtain a better understanding of the small-vessel radius-estimation results of others [1], [2], [3], [4] and it yields more accurate quantification. The accuracy of the new edge detector will be verified in Section 6.

The function $\alpha(\sigma\,\kappa_\Sigma)$, which avoids dislocation, is not invariant to the ratio between the principal isophote curvatures. α is not the same for a cylinder ($\kappa_2/\kappa_1 = 0$) and a ball ($\kappa_2/\kappa_1 = 1$). It is different for small values of $\sigma\kappa$ (e.g., for $\sigma\kappa$ smaller than 0.2). Therefore, a more general approximation for curved surfaces is presented in the next section.

4 Approximation for Curved Surfaces in 3D

Because α is not invariant to the ratio κ_2/κ_1, the sum of curvature components does not give enough information to correct for the dislocation of the curved surface. Therefore, not only the sum of curvature components, but also the ratio between the curvature components is used to correct for the dislocation. These two dimensionless parameters allow the creation of a two-dimensional look-up table in a limited domain, with $\sigma\,\kappa_\Sigma$ (that was used in the previous section) on one of the axis. An approximation of α as a function of $\sigma\kappa_\Sigma$ and κ_2/κ_1 is:

$$\alpha(\sigma\,\kappa_\Sigma, \frac{\kappa_2}{\kappa_1}) \approx -1 + \frac{\kappa_2^2}{2\,\kappa_1^2} + \left(\frac{3}{2} - \frac{\kappa_2^2}{2\,\kappa_1^2}\right) e^{\frac{(\sigma\kappa_\Sigma)^2}{4}\left(6.7 - 7.2\cdot 1.0374^{\left(\frac{5}{2}\cdot\frac{4\kappa_2}{\kappa_1}\right)^2}\right)}. \tag{16}$$

Equation (16) was obtained with a toroidal object (donut)—as a model of a curved vessel—stored in a discrete data set. For several values of the two radii of the toroid, we computed the corresponding value of α that produced the unbiased edge location and a function was fitted numerically through the values of α.

5 Implementation

In this section, the steps needed for implementation of the proposed method are described.

5.1 Implementation in 2D

Steps for implementation in 2D are listed below.

5.1.1 Derivatives

Separable Gaussian derivatives are used to calculate the first- and second-order derivatives of the image [11]. The blurring of the PSF and the Gaussian operators can be taken into account using: $\sigma = \sqrt{\sigma_{psf}^2 + \sigma_{op}^2}$.

5.1.2 Curvature

The derivatives are used to calculate L_w, L_{ww} and ΔL, using (4). After that, κ can be calculated using $\kappa = (L_{ww} - \Delta L)/L_w$. In edge regions, L_w will be larger than zero.

5.1.3 Zero Crossings

The zero crossings of the filter $L_{ww} - \alpha(\sigma\,\kappa)\,\kappa\,L_w$ must be detected to show the edges. To speed up the calculations, a 1D look-up table (LUT) can be used for α, indexed by the product of κ and σ (Fig. 2).

5.2 Implementation in 3D

Steps for implementation in 3D are listed below.

5.2.1 Derivatives

Gaussian derivatives are calculated. The total blurring is made isotropic in the x, y, and z-direction using $\sigma = \sqrt{\sigma_{psf}^2 + \sigma_{op}^2}$.

5.2.2 Curvature

The derivatives are used to calculate L_w, L_{ww}, and ΔL using (11). After that, κ_Σ can be calculated using $\kappa_\Sigma = (L_{ww} - \Delta L)/L_w$.

5.2.3 Zero Crossings

The zero crossings of the filter $L_{ww} - \alpha(\kappa_\Sigma\,\sigma)\,\kappa_\Sigma\,L_w$ must be detected to find the location of the surfaces.

- To detect spherical structures, use (15) to fill a 1D LUT, indexed by the product of κ_Σ and σ.
- To detect cylindrical structures (like vessels), use (8) to fill a 1D LUT, indexed by the product of κ_Σ and σ.
- If the ratio κ_2/κ_1 is not approximately 1 or 0, (16) can be used to fill a 2D LUT.

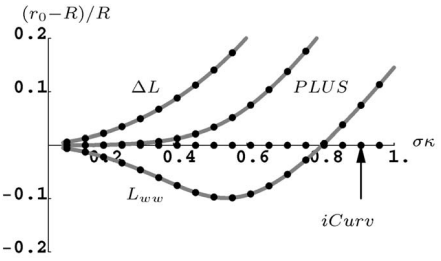

Fig. 4. Experimental (dots) and theoretical (curves) relative dislocation of L_{ww}, *PLUS*, ΔL, and the proposed method (*iCurv*). The dislocation of the proposed method is very small compared to the other methods.

The two principal components of the isophote curvature (κ_1 and κ_2), which can be used if the 3D object does not resemble a cylinder or a sphere, are derived from the equations in the article by van Vliet and Verbeek [19], which result in:

$$\begin{aligned}\kappa_G &= L_w^{-4}[L_x^2(L_{yy}L_{zz} - L_{yz}^2) + \\ &\quad L_y^2(L_{xx}L_{zz} - L_{xz}^2) + L_z^2(L_{xx}L_{yy} - L_{xy}^2) + \\ &\quad 2(L_yL_z(L_{xz}L_{xy} - L_{xx}L_{yz}) + L_xL_z(L_{yz}L_{xy} \\ &\quad - L_{yy}L_{xz}) + L_xL_y(L_{xz}L_{yz} - L_{zz}L_{xy}))] \\ \kappa_H &= \kappa_\Sigma/2 \\ \kappa_1 &= \kappa_H + \sqrt{\kappa_H^2 - \kappa_G} \\ \kappa_2 &= \kappa_H - \sqrt{\kappa_H^2 - \kappa_G}.\end{aligned} \tag{17}$$

The two principal components should be sorted by magnitude. Therefore, they must be swapped if κ_H is smaller than zero.

6 Experiments and Results

The proposed method was tested on synthetic images and on CT data to verify the accuracy and robustness of the algorithm. Synthetic images were obtained by first blurring a continuous object, then sampling, and, finally, adding white Gaussian noise. The CT data was obtained with a Philips Mx8000 IDT 16-slice CT scanner.

After creation of the images, the method proposed in this paper was used to locate the edges. The zero crossings were used to indicate the edge at subvoxel accuracy. We used continuous Gaussian derivatives to interpolate the blurred derivatives of the image (as shown by van den Boomgaard and van der Weij [20] and ter Haar Romeny [21]).

In the Section 6.1, an experiment is described to validate the theory and to make a comparison with other methods. In the Section 6.2, the results of the edge localization of small circular objects are shown to study the robustness for sampling. In Section 6.3, the sensitivity of the algorithm in the presence of noise is studied. In the Section 6.4, the behavior of the method on an image with varying curvature is shown. In Section 6.5, our approximation for objects in 3D that are not spherical or cylindrical is verified. Section 6.6 shows that the assumptions are valid for CT data, using quantitative measurements of a phantom. And, Section 6.7 shows that the method can be applied to the CT data of a real patient.

6.1 Localization Accuracy

An experiment was performed with a disk in a digitized 2D image to compare the location errors of various methods (Fig. 4). Equation (6) gives the theoretical dislocation. It can be seen that experimentally obtained results (dots) match the theory (curves). The dislocation of the proposed method is negligible compared to the other methods.

6.2 Sampled Image of Small Circular Object

Even for small disks, e.g., with the radius $R = 2$px (pixels), the method is able to locate edges with a relative dislocation $|r_0 - R|/R$ less than 10^{-8}, as shown in Fig. 5. This figure has been obtained

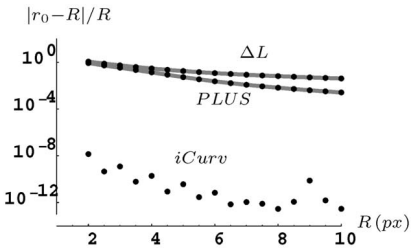

Fig. 5. Relative location error for disks in 2D with radius R from 2 to 10 pixels for $\sigma = 2.8$. Results of the experiment (dots) and theory (curves) are shown. The dislocation of the proposed method (*iCurv*) is much smaller than other methods.

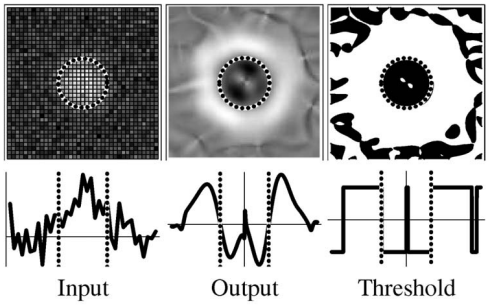

Fig. 6. Example of a noisy 2D image of a disk with radius $R = 6$ pixels and $SNR_i = 15.6\,dB$. Input, output of the proposed method and thresholded output are shown from left to right. The bottom row reflects a cross section through the center of the image of the top row. The output suppresses noise and the zero crossing is located with a small error.

with $\sigma_{psf} = 2$px and $\sigma_{op} = 2$px. It allows a comparison with the results of Verbeek and van Vliet [18]. A relative dislocation of 1 means that the radius is estimated twice as large as the actual radius. The dislocation of the proposed method is not exactly zero due to the limited working precision. The figure shows that the relative dislocation of the proposed method is much more accurate than ΔL, L_{ww}, and the *PLUS* operator. The relative dislocation is also much smaller than the generalized Radon transform [22].

6.3 Suppression of Noise

In order to test the robustness of the edge detector in the presence of noise, white Gaussian noise was added to the image of a disk (Fig. 6).

The second-order Gaussian-derivative kernels are analyzed to understand the relation between noise and dislocation before the results of the experiment are discussed.

The signal-to-noise ratio (*SNR*) in decibel is defined as:

$$SNR_{[dB]} = 20\,log_{10}\left(\frac{\mu_s}{\sigma_n}\right). \tag{18}$$

where μ_s is the mean signal amplitude and σ_n is the standard deviation of the noise. The relation between the standard deviation of the noise before (σ_{ni}) and after (σ_{no}) Gaussian filtering, for the D-order Gaussian derivative with N dimensions, is [23]:

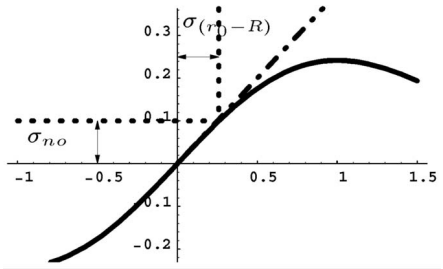

Fig. 7. A first-order approximation for the relation between the standard deviation of the noise σ_{no} and of the dislocation $\sigma_{(r_0-R)}$ is slope at the zero-crossing.

$$\left(\frac{\sigma_{no}}{\sigma_{ni}}\right)^2 = \int_{-\infty}^{\infty}\left(\frac{d^D\mathcal{G}}{dx^D}\right)^2 d\vec{x}, \tag{19}$$

This integral can be solved:

$$\left(\frac{\sigma_{no}}{\sigma_{ni}}\right)^2 = \frac{((2\,D)!)/(D!\,2^D)}{2^{N+D}\,\pi^{N/2}\,\sigma_{op}^{N+2D}}. \tag{20}$$

For a second-order Gaussian derivative kernel convolved with a step-edge, the slope at the zero-crossing is $d^2\mathcal{G}/dx^2\big|_{x=0}$. The first-order approximation for the relation between σ_{no} and the standard deviation of the dislocation $\sigma_{(r_0-R)}$ is given by this slope, as shown in Fig. 7.

$$\frac{\sigma_{no}}{\sigma_{(r_0-R)}} = \frac{d^2\mathcal{G}}{dx^2}\bigg|_{x=0} = \frac{1}{\sqrt{2\pi}\sigma_{op}^3} \Rightarrow \tag{21}$$

$$\sigma_{(r_0-R)} = \sqrt{2\pi}\,\sigma_{op}^3\,\sigma_{no}. \tag{22}$$

To find the relation between noise at the input and the dislocation, σ_{no} must be eliminated with (20).

The relative dislocation $(r_0 - R)/R$ as a function of the relative filter size $\sigma\kappa$ for various SNR_is is shown in Fig. 8. The results are based on five experiments. The relative dislocation as a function of the SNR_i for various σ_{op} is shown in Fig. 9. Both figures show a close correspondence between theoretical and experimental results. The other methods (L_{ww}, ΔL, and *PLUS*) let the systematic error raise for increasing scale. The proposed method is independent of scale in two-dimensional images. In three-dimensional images, the stochastic error is even lower, as shown by (20) and (22). The figures show that the systematic error is completely removed by the proposed method.

6.4 Slowly Varying Curvature

In this experiment, the curvature was not constant under the footprint of the Gaussian, but slowly varying. The edge-detection methods have been applied to an image with a filled ellipse (Fig. 10), which was blurred with $\sigma = 5$px at a 10-times higher resolution ($\sigma_{psf} = 0.5$px) to avoid sampling errors. The method of Mendonça et al. [17] was not tested in other experiments because the results are expected to be similar our results. This experiment shows a difference (Fig. 10) that can be explained by the location where the (nonconstant) curvature is estimated. His method is estimating the

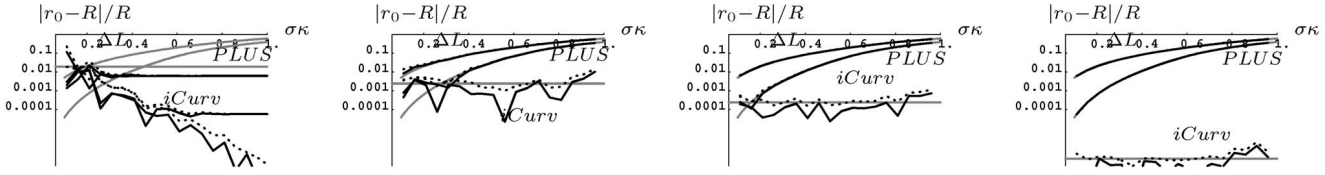

Fig. 8. Relative dislocation for a 2D image of a disk with $R = 25.5\,px$ as a function of $\sigma\kappa$ for various $SNR_i = \{4, 20, 40, 100\}\,dB$. Theory (gray), mean relative dislocation (black), and the sum of mean and standard deviation of the relative dislocation (black, dashed) are indicated for ΔL, *PLUS*, and *iCurv*.

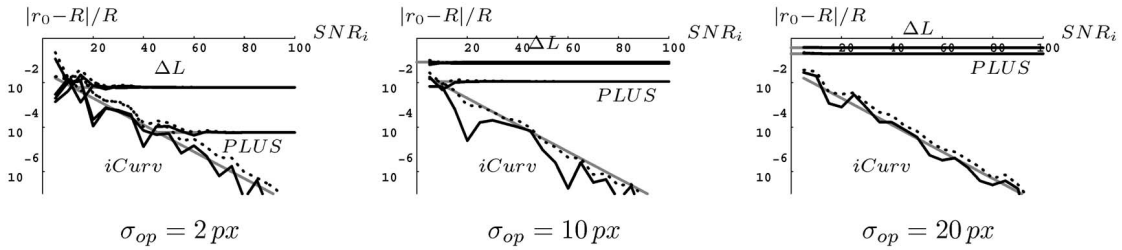

Fig. 9. Relative dislocation for a 2D image of a disk with $R = 25.5\,px$ as a function of SNR_i in decibel for various $\sigma_{op} = \{2, 10, 20\}\,px$. Theory (gray), mean relative dislocation (black), and the sum of mean and standard deviation of the relative dislocation (black, dashed) are indicated for ΔL, *PLUS*, and the proposed method (*iCurv*).

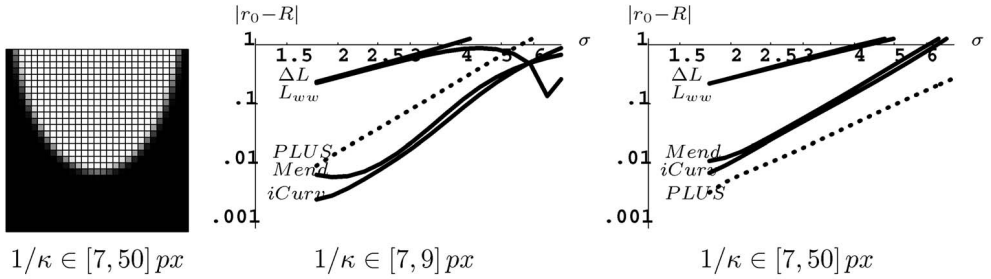

Fig. 10. A filled ellipse and the dislocation on its edge as a function of the total blurring. On the edge of the ellipse, the radius of curvature is slowly varying from 7 to 9 pixels and from 7 to 50 pixels. The method of Mendonça (*Mend*) was also included in this experiment. The dislocation was measured where the curvature is highest ($1/7\,px^{-1}$). For low change of curvature, our method (*iCurv*) performs best. For higher change of curvature, *PLUS* (dotted) performs best.

curvature far away from the true edge—at the zero-crossings of L_{ww}—while our filtering method does it everywhere—including the real edge location. In general, we can draw two conclusions from the experiments that we performed on ellipses. First, the total blurring σ has to remain smaller than $1/\kappa$ to avoid large dislocations. Second, the results give an indication that, for small changes in curvature our method performs best and, for larger changes in curvature, the *PLUS* operator performs best.

6.5 Toroidal Object

An experiment was performed to verify the quality of the approximation for three-dimensional objects that are not spherical or cylindrical. The result is shown in Fig. 11. The dislocation of our method is not zero because (16) is—in contrast to other equations in this paper—only an approximation. The figure shows that, especially in the range that is important for vessel quantification ($-0.5 < \kappa_2/\kappa_1 < 0.5$), the maximum dislocation of our method is small in comparison with others.

6.6 CT Data of Phantom

In order to show that our method can be applied to CT data and to perform quantitative measurements, a phantom was scanned of which the size is accurately known [24]. The labels and radii of the arteries represented in the three-dimensional cerebrovascular phantom are: vertebral (VA, 1.19mm), internal carotid (ICA, 1.75mm), and anterior, middle, and posterior-cerebral (ACA, 1.00mm; MCA, 1.39mm; PCA, 1.00mm) arteries (Fig. 12a). In the reconstructed volume, the voxel size is 0.30 and 0.3125 mm in the z and xy-directions, respectively, with a slice thickness of 1.5 mm. The spherical aneurysm in the center of the phantom and the integral of (12) were used to estimate the standard deviation of the PSF: $\sigma_{psf} = 0.66$ and 0.47mm in the z and xy-direction, respectively. The scales of the Gaussian derivatives were adjusted to make the total blurring isotropic with $\sigma = \sqrt{\sigma_{psf}^2 + \sigma_{op}^2} = 0.884$mm.

The edge detectors were all applied in 3D. For quantitative validation of the radius estimation, two-dimensional cross sections of the vessels were made. The eigenvectors of the Hessian were used to determine the orientation of the vessel. Cross sections were made at several locations and orientations. The estimated radii were averaged and the dislocations are summarized in Fig. 12b. The results show that our method performs better than ΔL and *PLUS*. For the vessels in this phantom, it does not perform much better than L_{ww} at this scale. The results also show that the proposed method reduces the bias and that the experimental points match the theory (curve in figure) within a 10 percent error range.

6.7 CT Data of Pulmonary Vessels

In this experiment, we verify the applicability of the method for the radius estimation of pulmonary vessels in contrast-enhanced CT data of a real patient. Fig. 13a shows a surface rendering of the data.

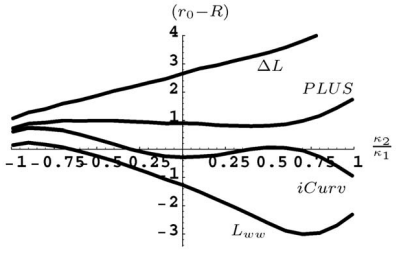

Fig. 11. Dislocation (in pixels) as a function of the ratio between κ_2 and κ_1 for a toroidal object ($\sigma = 8\text{px}, \sigma\kappa_\Sigma = \frac{1+\kappa_2/\kappa_1}{1.7}$).

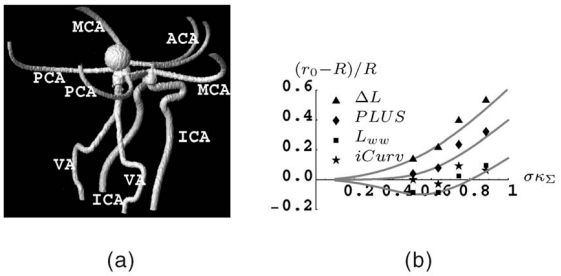

Fig. 12. CT data of vascular phantom. (a) Surface rendering. (b) Theoretical (curve) and experimental dislocation of the various edge-detection methods.

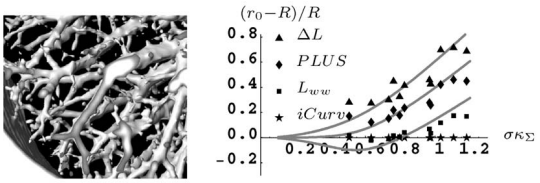

(a) (b)

Fig. 13. CT data of pulmonary vessels. (a) Surface rendering. (b) Theoretical (curve) and experimental dislocation of the various edge-detection methods.

In the reconstructed volume, the voxel size is 0.60 and 0.584 mm in the z and xy-directions, respectively, with a slice thickness of 1.3mm. The PSF can be approximated by a Gaussian: $\sigma_{psf} = 0.83$ and 0.76mm in the z and xy-direction, respectively. The total blurring is $\sigma = 1.393$mm.

In the patient data, we do not have a ground truth for the quantization of the vessel radius. Therefore, we assume that the dislocation of our method is zero. Fig. 13b shows the dislocation of the other methods relatively to our method.

The experimental points seem to match the theoretical curve well if we assume a 10 percent error range. Therefore, we can conclude that our method can be applied to CT data in order to estimate the radius of tubular objects without a bias.

7 Conclusion

The proposed method uses the locally measured isophote curvature to correct for the dislocation of a curved surface in 2D and 3D. It is a separable, noniterative filter operation that requires only one scale to locate edges of objects of different sizes, without surface extraction.

The Laplacian (ΔL), the second-order derivative in gradient direction (L_{ww}), and the *PLUS* operator show a systematic error for edges with locally constant curvature. Due to a mathematical derivation, we were able to design and implement an edge detector that removes the systematic error. The theory helps us to obtain a better understanding of the small-vessel radius-estimation results of others.

Because the systematic error is removed, the method is able to locate edges with locally constant curvature very accurately. The method is more accurate than conventional methods for circular, cylindrical, and spherical objects that are smaller than the footprint of the Gaussian PSF or with small sampled objects (e.g., radius of two pixels) and in the presence of noise or when the curvature is slowly varying, as was shown by the results.

To validate the assumptions (Section 3.2) for CT data, experiments were performed on the CT data of a phantom and a patient. The patient data showed that the radius of pulmonary vessels could be estimated within a 10 precent error range and the phantom data showed that our method detects edges without a bias.

All experimental results are in full agreement with the theory presented in this paper.

Future work may include an improvement of the solution for surfaces in 3D that are not cylindrical or spherical.

Acknowledgments

The authors would like to thank Annet Waaijer of the Universitair Medisch Centrum in Utrecht for the CT data of the phantom, Otto van Delden of the Academic Medical Center in Amsterdam for the CT data of the pulmonary vessels, Steven Lobregt and Roel Truyen of Philips Medical Systems in Best for discussions, and Remco Duits and Markus van Almsick of the Technische Universiteit Eindhoven for mathematical and software support.

References

[1] A.F. Frangi, W.J. Niessen, R.M. Hoogeveen, T. van Walsum, and M.A. Viergever, "Model-Based Quantitation of 3D Magnetic Resonance Angiographic Images," *IEEE Trans. Medical Imaging,* vol. 18, pp. 946-956, Oct. 1999.

[2] J.M. Reinhardt, N.D. d'Souza, and E.A. Hoffman, "Accurate Measurement of Intrathoracic Airways," *IEEE Trans. Medical Imaging,* vol. 12, no. 6, pp. 820-827, Dec. 1997.

[3] R.M. Hoogeveen, C.J.G. Bakker, and M.A. Viergever, "Limits to the Accuracy of Vessel Diameter Measurement in MR Angiography," *J. Magnetic Resonance Imaging,* vol. 8, pp. 1228-1235, 1998.

[4] K. Krissian, G. Malandain, and N. Ayache, "Model Based Multiscale Detection and Reconstruction of 3D Vessels," Research Report 3442, INRIA, Sophia Antipolis, France, 1998.

[5] K. Krissian, G. Malandain, N. Ayache, R. Vaillant, and Y. Trousset, "Model Based Multiscale Detection of Tubular Structures in 3D Images," Research Report 3736, INRIA, Sophia Antipolis, France, 1999.

[6] G.M.P. van Kempen and L.J. van Vliet, "The Influence of the Regularization Parameter and the First Estimate on the Performance of Tikhonov Regularized Non-Linear Image Restoration Algorithms," *J. Microscopy,* vol. 198, no. 1, pp. 63-67, 2000.

[7] J. Llacer and J. Nuñez, "Ghost Images and Feasibility of Reconstructions with the Richardson-Lucy Algorithm," *SPIE Proc.,* vol. 2302, pp. 207-221, 1994.

[8] A.S. Carasso, "Linear and Nonlinear Image Deblurring: A Documented Study," *SIAM J. Numerical Analysis,* vol. 36, no. 6, pp. 1659-1689, 1999.

[9] H. Bouma, "Detection of Edges in an Image," European Patent 04101027.3, Mar. 2004.

[10] E.L. Nickoloff and R. Riley, "Simplified Approach for Modulation Transfer Function Determination in Computed Tomography," *Medical Physics,* vol. 12, pp. 437-442, July 1985.

[11] M. Nielsen, L.M.J. Florack, and R. Deriche, "Regularization, Scale-Space and Edge-Detection Filters," *J. Math. Imaging and Vision,* vol. 7, no. 4, pp. 291-307, 1997.

[12] S. Doré and Y. Goussard, "Experimental Determination of CT Point-Spread Function Anisotropy and Shift-Variance," *Proc. IEEE Eng. in Medicine and Biology Soc.,* vol. 19, pp. 788-791, Oct. 1997.

[13] J.F. Canny, "A Computational Approach to Edge Detection," *IEEE Trans. Pattern Analysis and Machine Intelligence,* vol. 8, pp. 679-698, Nov. 1986.

[14] D. Marr and E. Hildreth, "Theory of Edge Detection," *Proc. Royal Soc.,* pp. 187-217, 1980.

[15] K. Ottenberg, "Model-Based Extraction of Geometric Structure from Digital Images," PhD dissertation, Utrecht Univ., The Netherlands, Nov. 1993.

[16] L.J. van Vliet and P.W. Verbeek, "Edge Localization by MoG Filters: Multiple-of-Gaussians," *Pattern Recognition Letters,* vol. 15, pp. 485-496, May 1994.

[17] P.R.S. Mendonça, D. Padfield, J. Miller, and M. Turek, "Bias in the Localization of Curved Edges," *Proc. European Conf. Computer Vision,* part 2, pp. 554-565, May 2004.

[18] P.W. Verbeek and L.J. van Vliet, "On the Location Error of Curved Edges in Low-Pass Filtered 2D and 3D Images," *IEEE Trans. Pattern Analysis and Machine Intelligence,* vol. 16, no. 7, pp. 726-733, July 1994.

[19] L.J. van Vliet and P. Verbeek, "Curvature and Bending Energy in Digitized 2D and 3D Images," *Proc. Scandinavian Conf. Image Analysis,* pp. 1403-1410, 1993.

[20] R. van den Boomgaard and R. van der Weij, "Gaussian Convolutions, Numerical Approximations Based on Interpolation," *Proc. Scale-Space and Morphology in Computer Vision,* vol. 3, pp. 205-214, July 2001.

[21] B.M. ter Haar Romeny, *Front-End Vision and Multi-Scale Image Analysis.* The Netherlands: Kluwer Academic, 2002.

[22] C.L. Luengo Hendriks, M. van Ginkel, P.W. Verbeek, and L.J. van Vliet, "The Generalized Radon Transform: Sampling and Memory Consideration," *Proc. Computer Analysis of Images and Patterns (CAIP),* vol. 2756, pp. 681-688, 2003.

[23] F. van der Heijden, *Image Based Measurement Systems: Object Recognition and Parameter Estimation.* Chichester, U.K.: John Wiley and Sons, 1994.

[24] R. Fahrig, A.J. Fox, and D.W. Holdsworth, "A Three-Dimensional Cerebrovascular Flow Phantom," *Medical Physics,* vol. 26, no. 8, pp. 1589-1598, Aug. 1999.